REVIEW

Check for updates

Quasi-2D halide perovskite crystals and their optoelectronic applications

Xin Sheng,[ab] Yahui Li,[b] Ming Xia[b] and Enzheng Shi ⓘ *[b]

Due to the widely tunable and exceptional semiconductor properties, quasi-two-dimensional (2D) halide perovskites have been considered outstanding candidates for next-generation optoelectronic devices and have thus undergone rapid development over the last decade. Their property tunability is intimately correlated with the quantum-well thickness (corresponding to the *n* value, the number of octahedral layers in each layer of quasi-2D halide perovskites). However, a systematic review of the relationship between the *n* value and the optoelectronic properties/applications of the quasi-2D perovskites is lacking. In this review, we begin with the *n*-dependent properties of quasi-2D perovskites, and move on to the synthesis of different forms of quasi-2D perovskite crystals. Afterwards, we focus on the existing optoelectronic applications using quasi-2D perovskites including light-emitting diodes, solar cells, lasers, and photodetectors. In the last section, we discuss the current challenges and a few promising directions with a special focus on the precise control of the *n* value. Moreover, the possible non-centrosymmetrical ordering of the organic ligands in quasi-2D halide perovskites provides new insights and opportunities to study the interaction between spontaneous polarization, photovoltaic effect, and carrier transport behaviors in the corresponding electronic and optoelectronic devices.

1. Introduction

The last decade has witnessed the explosive development of layered halide perovskites in high-performance optoelectronic devices (solar cells,[1–5] light-emitting diodes,[6–10] lasers,[11–15]

[a]School of Materials Science & Engineering, Zhejiang University, Hangzhou, 310027, China
[b]School of Engineering, Westlake University, Hangzhou, 310024, China. E-mail: shienzheng@westlake.edu.cn

Enzheng Shi is currently an assistant professor at the School of Engineering, Westlake University. Dr Shi received his bachelor's degree from Shandong University in 2010 and PhD degree from Peking University in 2015. He worked as a postdoc research associate in Iowa State University from 2015 to 2017, and in Purdue University from 2017 to 2020, respectively. His research interests cover two aspects: (1) design, synthesis, and applications of novel electronic materials and heterostructures; and (2) assembly and manipulation of low-dimensional carbon nanomaterials.

photodetectors,[16–20] *etc.*) due to their marvelous optoelectronic properties and high stability.

Layered halide perovskites consist of metal halide octahedra sandwiched by symmetrical layers of organic ligands. According to the variation in organic ligands, they can be generally classified into three types:[21–25] Ruddlesden–Popper (RP) phase,[26] Dion–Jacobson (DJ) phase[27,28] and alternating cations in the interlayer space (ACI) phase.[29] The common expression of the RP phase is $L_2A_{n-1}M_nX_{3n+1}$, where L stands for large organic ammonium cations, A for small cations (*e.g.*, Cs^+, $CH_3NH_3^+$ (MA^+) and $CH_3(NH_2)_2^+$ (FA^+)), M for divalent metals like Pb^{2+}, and X for halogen anions (I^-, Br^- and Cl^-). In addition, the number of octahedral layers in each layer of 2D halide perovskites is specified by another unique parameter, *n*. 2D perovskites with $n = 1$ and $n > 1$ (high *n*) can also be designated as pure-2D and quasi-2D perovskites, respectively.

The major distinction between RP phase, DJ phase and ACI phase perovskites originates from the large organic ligand L (Fig. 1a). In the RP phase, monoammonium cations are used as large organic ligands and the adjacent layers are connected by van der Waals force. The molecular structure of several reported ligands is listed in Fig. 1b. In the DJ phase, however, diammonium cations are applied to chemically link adjacent layers together, making mechanical exfoliation of DJ phase perovskites into molecularly thin sheets impossible. ACI phase halide perovskites are considered to combine the RP phase's chemical formula and the DJ phase's structural properties.[30] Despite the fact that the ACI phase is supposed to have better performance,

This journal is © The Royal Society of Chemistry 2022

J. Mater. Chem. A, 2022, **10**, 19169–19183 | 19169

Fig. 1 Structure of 2D halide perovskites. (a) Schematic representation of Ruddlesden−Popper (RP) phase, Dion−Jacobson (DJ) phase and alternating cations in the interlayer space (ACI) phase 2D perovskites. (b) Some ligands employed in RP phase 2D perovskites.

a complete grasp of its intrinsic properties remains unclear due to the lack of investigation into single crystals. Due to the ease of mechanical exfoliation into thin sheets, molecularly flat surface and no dangling bonds at the surface, RP phase perovskites are the most well-investigated among the three types of layered perovskites mentioned above and thus will be mainly discussed in this review.

One merit of 2D halide perovskites is their wide property tunability resulting from facile and flexible composition engineering.[31–36] They can be substituted completely or partially by other similar ions. Additionally, adjusting the n value has a significant impact on their optoelectronic properties. Reports indicate that quasi-2D perovskites combine the enhanced stability of pure-2D perovskites with the superior carrier mobility of their 3D counterparts, and optoelectronic devices based on quasi-2D perovskites outperform those based on pure-2D perovskites.[37] Though quasi-2D perovskites show attractive properties and promising applications, their systematic summary is rarely seen.

In this review, we'll focus on the properties, synthesis and applications of RP phase quasi-2D perovskites ($n > 1$). We begin with emphasizing the dependence of semiconductor properties on the n value. Then the synthesis methodologies of quasi-2D perovskites in various crystal forms are summarized. The next section covers optoelectronic applications, such as light-emitting diodes, solar cells, lasers, and photodetectors. Finally, we summarize the current challenges and outlook of the quasi-2D perovskites.

2. Properties

2.1 Quantum and dielectric confinement

2D halide perovskites could be considered as quantum wells formed by sandwiching octahedral layers by organic ligand layers in the out-of-plane direction.[38–40] Typically, the band gap of the insulating organic ligand layer is substantially larger than that of the octahedral layer, thus forming type-I band alignment. As a result, the excited electrons and holes will be

confined in the octahedral layer. Quantum confinement and dielectric screening effects have a huge impact on the charge carrier behaviours of 2D perovskites,[41–44] which is directly correlated with the thickness of the quantum wells (n value). As n increases, the coupling effect between the electrons and holes weakens, leading to an increase in exciton transport distance and drop in exciton density and binding energy[45] (Fig. 2a).

In 2D halide perovskites, effective high-frequency dielectric coefficients will increase as n increases. Taking the $BA_2MA_{n-1}Pb_nI_{3n+1}$ (n = 1–7) series for example, the computed high-frequency dielectric constant (ε_∞) along the out-of-plane direction is around 5.8 for octahedral layers and around 2.0 for organic layers[46] (Fig. 2b). With the increase of the n value, the contribution of octahedral layers to the effective high-frequency dielectric coefficient increases, resulting in a rise in the effective high-frequency dielectric coefficient[46] (Fig. 2c). Fig. 2c also shows the mathematical expression for this regulation, where ε_b is the high-frequency dielectric constant of the organic layer component, L_b is the length of the organic layer component, ε_w is the high-frequency dielectric constant of the inorganic layer component, and L_w is the length of the inorganic layer component.

2.2 Optical properties

The n-dependent optical properties can be characterized roughly by absorption spectroscopy and photoluminescence (PL) spectroscopy. For 2D perovskites with strong exciton absorption, the Tauc plot method is commonly used to extract the corresponding optical band gap from UV-vis absorption spectra.[47] Due to the quantum confinement and dielectric screening effects, the band gap of quasi-2D halide perovskites will decrease with n value. The optical band gap of $(BA)_2PbI_4$ is 2.42 eV, as shown in Fig. 2d, and drops to 1.85 eV for $(BA)_2MA_4Pb_5I_{16}$.[48]

Consistent with the UV-vis spectra, the PL emission peaks of 2D perovskites also change with n value (Fig. 2e).[48] In the $BA_2MA_{n-1}Pb_nI_{3n+1}$ series, the PL emission redshifts from green ($\sim$520 nm for $(BA)_2PbI_4$) to red (680 nm for $(BA)_2MA_4Pb_5I_{16}$) as the n value increases from 1 to 4. In addition, the PL peaks of n = 6 and n = 7 could further red-shift to around 700 nm and 713 nm, respectively.[46] Because of the self-absorption in bulk crystals, the PL intensity of monolayers is frequently stronger than that of the bulk for a quasi-2D perovskite with a given n value.[17]

The PL efficiency of 2D perovskites relies on several factors, one of which is electron–phonon coupling. As the lattice of 2D perovskites is quite soft, the interaction of phonons and electrons is more pronounced.[49] The PL efficiency will be significantly affected by the strength and mechanism of electron–phonon coupling,[50] which can be obtained by analysing temperature-dependent PL spectra[51] (Fig. 2f). As revealed by the density functional theory (DFT) calculation, the rigidity of the organic ligands also plays an important role in the electron–phonon interaction. With enhanced rigidity of the organic ligands in 2D halide perovskites, the structure fluctuation of the perovskite will be suppressed, resulting in reduced exciton–phonon coupling and increased PL efficiency.[52]

19170 | *J. Mater. Chem. A*, 2022, **10**, 19169–19183

This journal is © The Royal Society of Chemistry 2022

Fig. 2 Quantum-well structure of RP phase perovskites and their optical properties as well as surface morphology. (a) Quantum-well structure of layered perovskites[45] (Copyright: 2021, Light: Science & Applications). (b) Calculated high-frequency dielectric constant of $(BA)_2(MA)_5Pb_7I_{22}$ in the stacking direction[46] (Copyright: 2019, Proceedings of the National Academy of Sciences of the United States of America). (c) Relationship between the effective high-frequency dielectric constant and n value[46] (Copyright: 2019, Proceedings of the National Academy of Sciences of the United States of America). (d) Absorption and (e) PL spectra of $BA_2MA_{n-1}Pb_nI_{3n+1}$ ($n = 1-5$)[48] (Copyright: 2020, Nature Communications); (f) temperature dependent PL of $(BA)_2MA_4Pb_5I_{16}$ (ref. 51) (Copyright: 2019, The Journal of Physical Chemistry Letters). (g) Q-Plus non-contact AFM image at room temperature of $(BA)_2MA_3Pb_4I_{13}$ (scale bar: 1 nm)[17] (Copyright: 2018, Nature Materials). (h) Schematic surface structure after relaxation.[53] (i) Atomic-resolution STM image of $(BA)_2MA_3Pb_4I_{13}$ (scale bar: 2 nm) and (j) relative simulated charge density plot[53] (Copyright: 2022, Nature Communications).

2.3 Surface state

The material surface generally possesses distinct properties compared with the bulk regions. To study the surface states without the effect from the bulk states, Leng *et al.*[17] employed monolayer crystals obtained by mechanical exfoliation. The surface of the exfoliated perovskite $(BA)_2MA_3Pb_4I_{13}$ is initially a well-ordered periodic square lattice with minimal density of holes and defects, according to the high-resolution atomic force microscopy (AFM) characterization[17] (Fig. 2g). Upon heating, the organic cation at the surface will reorient, which will have a direct impact on the PL emission. This impact weakens with the increase of the n value.

Apart from high-resolution AFM, scanning tunnelling microscopy (STM) is another tool to directly visualize the surface states. Shao *et al.*[53] proposed a model based on mono-layer $(BA)_2MA_3Pb_4I_{13}$ perovskites, suggesting that the stronger out-of-plane tilt of adjacent Pb–I octahedra toward each other will naturally push their apical I atoms closer, forming a "dimer-like" structure eventually (Fig. 2h). The obtained STM image of $(BA)_2MA_3Pb_4I_{13}$ (Fig. 2i) demonstrated a clear dimer structure corresponding to the iodine atom at the top, which is further verified by the simulated charge density image[53] (Fig. 2j).

2.4 Transport behaviours

With strongly bound excitons and tunable band structures, quasi-2D perovskites are ideal candidates for optoelectronic applications, where exciton transport and annihilation are two key processes. Deng *et al.*[48] employed transient absorption microscopy to quantify the n-dependent exciton diffusion and annihilation in perovskites with different n values, revealing the key role of electron–hole interaction and dielectric screening. For $BA_2MA_{n-1}Pb_nI_{3n+1}$, the exciton diffusion constant increases as the quantum well becomes thicker, ranging from 0.06 to 0.34 $cm^2\ s^{-1}$, resulting in exciton diffusion in the hundreds of nanometre range[48] (Fig. 3a). With increasing n value, the rate of exciton annihilation decreases[48] (Fig. 3b). The combination of long exciton transport distance and slow annihilation rate highlights the unique properties of 2D perovskites as exciton-like optoelectronic materials. In addition, the exciton annihilation rate in 2D halide perovskites is orders of magnitude lower than that of monolayer transition metal dichalcogenides.[54]

Due to the layered structure, the electronic properties of quasi-2D halide perovskites are anisotropic. Using the space charge current limiting approach, Wang *et al.*[55] investigated the in-plane and out-of-plane charge transport properties of
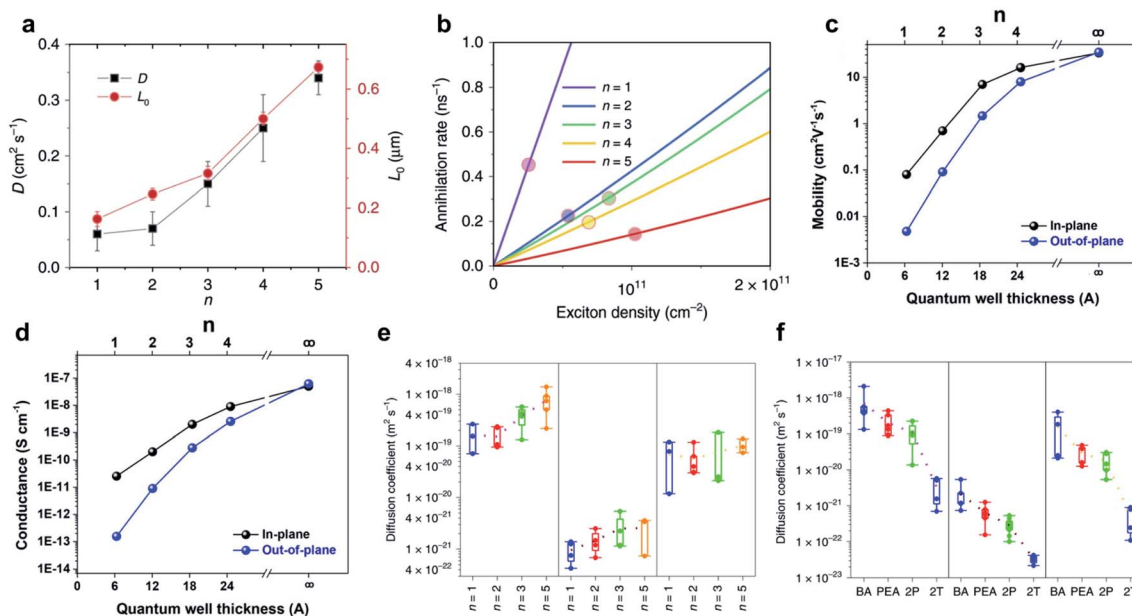
This journal is © The Royal Society of Chemistry 2022

J. Mater. Chem. A, 2022, **10**, 19169–19183 | **19171**

Fig. 3 Carrier behaviour in 2D perovskites. (a) Diffusion constant, (b) annihilation rate[48] (Copyright: 2020, Nature Communications), (c) mobility and (d) conductance[55] (Copyright: 2018, ACS Nano) as a function of n value in the $(BA)_2MA_{n-1}Pb_nI_{3n+1}$ series. Comparison of the impact of (e) the n value and (f) ligands on the halogen diffusion constant. Left, Fickian diffusion coefficients; middle, non-Fickian diffusion coefficients; right, diffusion coefficients by KMC simulation[56] (Copyright: 2021, Nature Nanotechnology).

$BA_2MA_{n-1}Pb_nI_{3n+1}$. The in-plane properties were studied by vapor-plating two electrodes on one side while the out-of-plane properties were studied by vapor-plating two electrodes on opposite sides. Both the carrier mobility and electrical conductivity increase in both in-plane and out-of-plane directions as the n value increases. Because of the organic barriers and van der Waals interaction along the out-of-plane direction, the in-plane carrier mobility and electrical conductivity are always higher than those along the out-of-plane direction (Fig. 3c and d). However, the discrepancies between these properties along the two directions decrease as the n value increases, indicating the reduced anisotropy for high-n quasi-2D halide perovskites.[55]

In addition to the motion of charge carriers, the organic ligands and n value in the 2D halide perovskites also have a significant impact on the ion motion within the soft lattice. For instance, by assembling vertical heterostructures between different 2D halide perovskites, Akriti *et al.*[56,57] investigated the influence of the n value and ligands on anionic diffusion. The vertical heterostructures are made up of a top iodide perovskite and bottom bromide perovskite. Upon varying the n value of the top $BA_2MA_{n-1}Pb_nI_{3n+1}$ from 1 to 5, the anionic diffusion coefficient increases gradually according to three different independent diffusion models, suggesting faster halide migration in higher n perovskites (Fig. 3e). When it comes to the effect of organic cations, it was discovered that bulkier π-conjugated ligands like bithiophenylethylammonium (2T) are more effective in preventing halide diffusion than benzene-based π-conjugated systems or short-chain aliphatic ligands, implying that molecular engineering and dimensional engineering could be helpful to effectively suppress anionic diffusion (Fig. 3f).

3. Synthetic strategies

Quasi-2D perovskites can be synthesized in different forms. In this section, we will summarize the synthesis methodologies for quasi-2D perovskite single crystals, nanosheets and thin films, and discuss the existing challenges in crystal synthesis.

3.1 Bulk single crystals

Quasi-2D halide perovskite single crystals are essential to determine their crystal structure and investigate their intrinsic properties due to their low density of defects and impurities. To synthesize phase-pure quasi-2D halide perovskite single crystals with precise control of the n value, a deep understanding of 2D halide perovskite single crystals as well as their growth mechanism is of great significance.

To grow quasi-2D halide perovskite single crystals, various techniques have been developed. The slow-cooling method (Fig. 4a) is one of the widely utilized strategies, in which the precursors are first added to the solvent (typically mixed acids containing hydroiodic/hydrobromic acid and hypophosphorous acid). After that, the solution will be heated to dissolve the precursors until it becomes clear. In the process of cooling, the supersaturation of the halide perovskites in the solution causes the nucleation of the desired phase. The final quasi-2D halide perovskite bulk crystals will be collected until the solution reaches room temperature. Using this method, $BA_2MA_{n-1}Pb_nI_{3n+1}$ $(n = 1–4)$[58] were synthesized with centimeter size, followed by the $n = 5$ (ref. 59), 6 and 7 (ref. 46 and 60) counterparts (Fig. 4b).

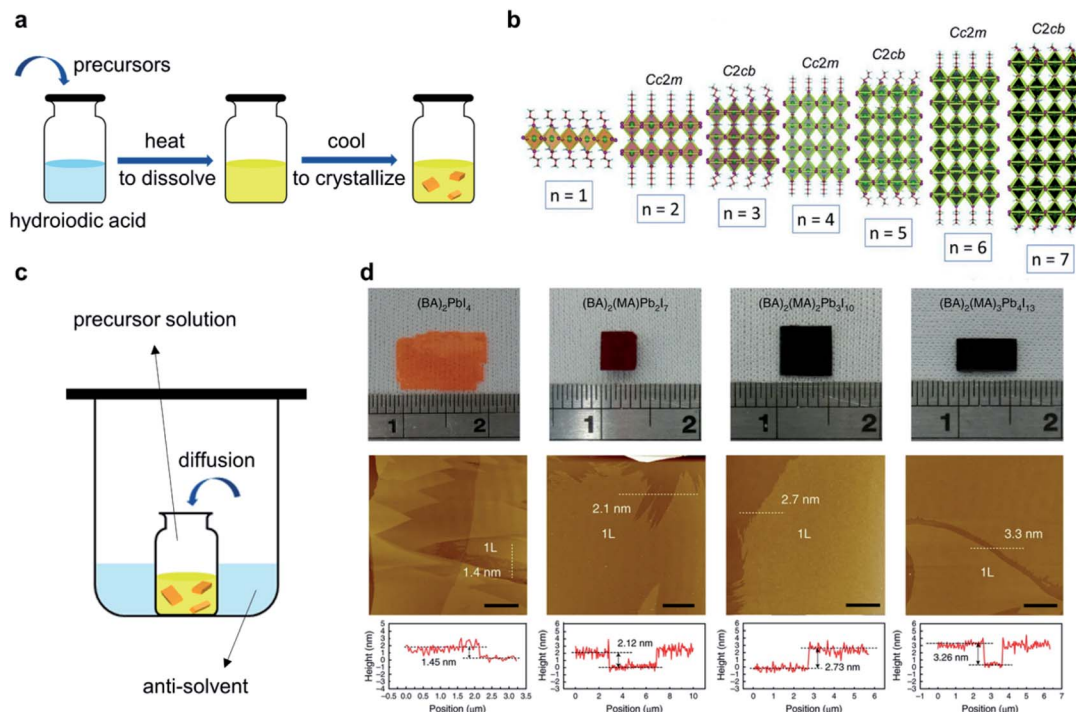Additional methods for synthesis of quasi-2D halide perovskite bulk crystals include anti-solvent diffusion,[68] slow

19172 | *J. Mater. Chem. A*, 2022, **10**, 19169–19183

This journal is © The Royal Society of Chemistry 2022

Fig. 4 Growing methods of bulk single crystals. (a) Schematics of the slow-cooling method. (b) Crystal structure of $BA_2MA_{n-1}Pb_nI_{3n+1}$ ($n = 1–7$)[46] (Copyright: 2019, Proceedings of the National Academy of Sciences of the United States of America). (c) Schematics of the anti-solvent diffusion method. (d) Optical images of BA_2PbI_4, $BA_2MAPb_2I_7$, $BA_2MA_2Pb_3I_{10}$ and $BA_2MA_3Pb_4I_{13}$ bulk crystals and corresponding AFM images (scale bars: 4 μm)[17] (Copyright: 2018, Nature Materials).

evaporation,[63,77] temperature-gradient-controlled[72] and space-confined methods.[64] For example, Cinquino et al.[68] applied an anti-solvent crystallization method (Fig. 4c) and successfully synthesized $DA_2MAPb_2I_7$ single crystals by adopting γ-butyrolactone as the solvent and diethyl ether as the anti-solvent. Raghavan et al.[63] applied a slow evaporation strategy under constant-temperature conditions to grow millimeter-scale BA_2-$MA_{n-1}Pb_nI_{3n+1}$ ($n = 1–3$) single crystals. Wang et al.[70] employed a method that combined a slow-cooling method and chemical vapor deposition (CVD) method and successfully synthesized bulk crystal heterostructures both laterally and vertically with different n values. A summary of representative as-synthesized bulk 2D halide perovskite single crystals from different methods is presented in Table 1.

Even though quasi-2D halide perovskite bulk single crystals with determined n values from 1–7 have already been experimentally synthesized, it is still very challenging to get phase-pure quasi-2D halide perovskite crystals with a high n value once the composition is changed, such as using a different halide anion or rigid bulky organic ligand. For the as-existing methods, the common strategy to control the n purity is to adjust the molar ratio of different precursors, which is quite tricky and requires a lot of trial and error. And the molar ratio between different ions in the final recipe is far from the stoichiometric ratio of the desired phase.

Based on the quasi-2D halide perovskite bulk single crystals, mechanical exfoliation could be applied to reduce the thickness of the layered structure and obtain few-layer even monolayer crystals, providing a platform to investigate the surface properties. By mechanical exfoliation, Leng et al.[17] obtained BA_2-$MA_{n-1}Pb_nI_{3n+1}$ ($n = 1–4$) monolayer crystals (Fig. 4d) and found reversible order–disorder surface transition of perovskites under laser annealing.

3.2 Nanosheets

Quasi-2D halide perovskite nanosheets are another widely investigated crystal form. Herein, the thin nanosheets mainly refer to single crystals with well-defined geometry and thickness within 100 nm that are prepared by direct synthesis. Without grain boundaries, nanosheets are also essential platforms to investigate their electronic and optoelectronic properties. Similar to exfoliated thin crystals, the thickness of nanosheets can be reduced to as thin as a monolayer. However, nanosheets generally possess the superiority of being able to precisely control their shape, size, and thickness through growth conditions, and the direct synthetic strategy also facilitates the preparation and further study of thin pure-2D and quasi-2D halide perovskites with strong van der Waals interaction (like strong π–π stacking between layers).

The direct solution synthesis of 2D halide perovskite nanosheets was first reported by Dou et al.[78] The basic synthetic procedure is depicted in Fig. 5a. Precursors are dissolved in a mixture of anhydrous dimethylformamide, acetonitrile and chlorobenzene. Then a diluted drop of precursor solution was dropped on preheated substrates. After the evaporation of solvent, atomically thin $(BA)_2PbBr_4$ nanosheets can be obtained.

Table 1 2D perovskite bulk single crystals and their synthesis method

Composition	n value	Growth methods	Ref.
$BA_2MA_{n-1}Pb_nI_{3n+1}$	1, 2	Cooling method	61
	2	Cooling method	62
	1, 2, 3	Slow evaporation method	63
	3	Space-confined method	64
	1, 2, 3, 4	Cooling method	17, 55 and 58
	2, 3, 4	Cooling method	65
	1, 2, 3, 4, 5	Cooling method	66
	5	Cooling method	59
	6, 7	Cooling method	46
$BA_2(GA)_{n-1}Pb_nI_{3n+1}$	2	Cooling method	62
$BA_2(DMA)_{n-1}Pb_nI_{3n+1}$	2	Cooling method	62
$(C_5H_{11}NH_3)_2MA_{n-1}Pb_nI_{3n+1}$	2	Cooling method	65 and 67
$(C_6H_{13}NH_3)_2MA_{n-1}Pb_nI_{3n+1}$	2	Cooling method	65
$(C_{12}H_{25}NH_3)_2MA_{n-1}Pb_nI_{3n+1}$	1, 2	Anti-solvent diffusion method	68
	2, 3, 4, 5	Cooling method	69
$PEA_2MA_{n-1}Pb_nI_{3n+1}$	1, 2	Cooling method	70
	1, 2, 3	Cooling method	71
$BA_2FA_{n-1}Pb_nI_{3n+1}$	2	Cooling method	62
$BA_2(MA_xFA_{1-x})_{n-1}Pb_nI_{3n+1}$	2	Temperature-gradient-controlled method	72
$BA_2MA_{n-1}Pb_nBr_{3n+1}$	1, 2	Cooling method	70
	3	Cooling method	73
$BA_2FA_{n-1}Pb_nBr_{3n+1}$	2	Cooling method	74
$(C_mH_{2m+1}NH_3)_2MA_{n-1}Pb_nBr_{3n+1}$ ($m = 6\text{--}8$)	2	Cooling method	75
$(CH_3OC_3H_9N)Cs_{n-1}Pb_nBr_{3n+1}$	**2**	**Cooling method**	**76**

By replacing the iodine with other halogens in the precursors, $(BA)_2PbCl_4$ and $(BA)_2PbI_4$ nanosheets can also be synthesized. Following a similar method, Gao *et al.*[39] and Shi *et al.*[79] synthesized a series of 2D halide perovskite nanosheets including $(2T)_2PbI_4$ (2T: bithiophenylethylammonium), $(BTm)_2PbI_4$ (BTm: 2-(4′-methyl-5′-(7-(3-methylthiophen-2-yl)benzo[c][1,2,5]thiadiazol-4-yl)-[2,2′-bithiophen]-5-yl)ethan-1-aminium), $(4Tm)_2PbI_4$ (4Tm: quaterthiophenylethylammonium), *etc.* using a series of bulky conjugated organic ligands

and lead-free $(2T)_2SnI_4$ and $(4Tm)_2SnI_4$, *etc.* using different metal cations. By epitaxially growing one type of 2D halide perovskite directly along the edge of one pre-synthesized template thin sheet, the 2D halide perovskite epitaxial heterostructure has also been realized with a rich composition tunability (Fig. 5b).

In order to directly synthesize quasi-2D nanosheets with $n > 1$, Pan *et al.*[80] established a method which derived from a slow cooling method for bulk crystal growth. A series of large-area
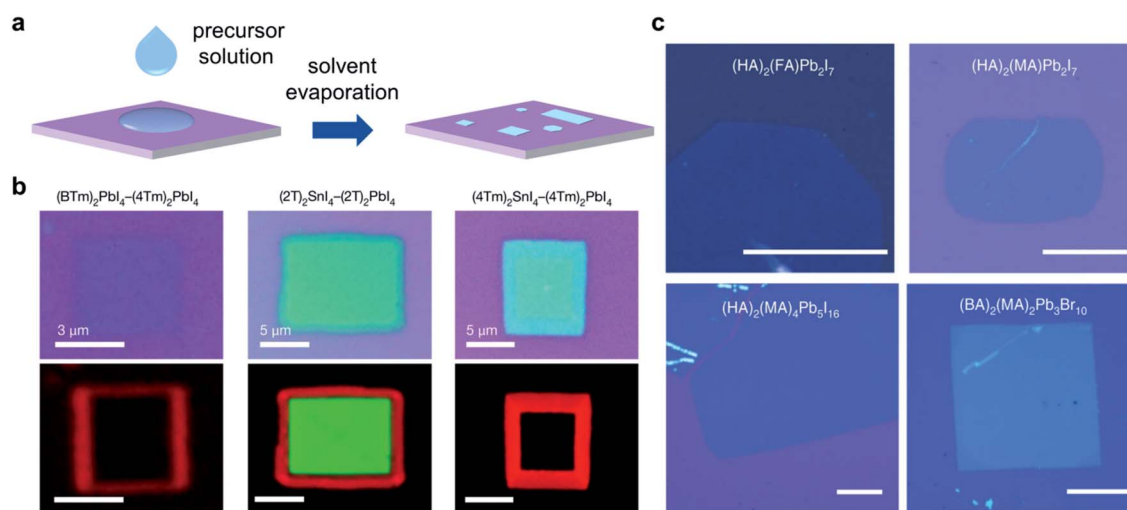

Fig. 5 Synthesis and morphology of perovskite nanosheets. (a) Schematic illustration of direct synthesis of 2D halide perovskite thin sheets. (b) Optical and PL images of $(BTm)_2PbI_4$-$(4Tm)_2PbI_4$, $(2T)_2SnI_4$-$(2T)_2PbI_4$ and $(4Tm)_2SnI_4$-$(4Tm)_2PbI_4$ heterostructures[79] (Copyright: 2020, Nature). (c) Optical images of $HA_2FAPb_2I_7$, $HA_2MAPb_2I_7$, $HA_2MA_4Pb_5I_{16}$ and $BA_2MA_2Pb_3Br_{10}$ nanosheets (scale bars: 25 µm)[80] (Copyright: 2021, Nature Nanotechnology).

quasi-2D perovskite nanosheets with tunable compositions and well-defined shape were obtained (Fig. 5c). By transferring a small droplet of supernatant precursor solution (for quasi-2D halide perovskite bulk single crystals) onto a glass substrate, nucleation and growth of nanosheets happened immediately at the solution surface. The lateral scale of the as-grown quasi-2D perovskite nanosheets can reach tens of micrometres and sometimes even above 100 μm. These large-area and thin quasi-2D halide perovskite nanosheets were used to assemble a series of van der Waals heterostructures. Based on these hetero-structures, the carrier diffusion across the interface was studied, implying that carriers would transfer from a lower n phase to a higher n phase due to the type-I band alignment.

In addition to the above solution-processing strategies,[81] the chemical vapor deposition (CVD) method, which is a conventional way to obtain ultrathin 2D materials like transition metal dichalcogenides and graphene, offers another alternative. Chen *et al.*[82] successfully transformed pure-2D BA_2PbBr_4 ($n = 1$) into quasi-2D $BA_2MA_{n-1}Pb_nBr_{3n+1}$ ($n > 1$) crystals through a CVD process. During this process, however, the MA cations are intercalated inside the perovskite lattice, introducing a very high density of lattice defects.

3.3 Thin films

Compared with bulk single crystals and nanosheets, quasi-2D halide perovskite thin films are most extensively utilized in electronic and optoelectronic devices. This is because of their ease in fabricating large-area, thickness-controllable thin film, which is compatible with the fabrication process of thin-film solar cells, LEDs and transistors.

To make quasi-2D halide perovskite thin films, spin-coating and blade-coating processes are two common routes, as shown schematically in Fig. 6a and b. Distinct from single crystals and nanosheets, the phases in thin films are more complicated due to their polycrystalline nature. One thing that needs to be noted is that quasi-2D halide perovskite thin films consist of mixed 2D perovskite phases with different n values. The claimed n value of quasi-2D halide perovskite thin films in the reported literature always denotes the dominating n value or is determined by the stoichiometry of the added precursors. As shown in Fig. 6c, the absorption spectra of thin films possess multiple peaks compared with those of exfoliated single crystals. For example, the absorption spectra of $(BA)_2MA_2Pb_3I_{10}$ ($n = 3$) thin films exhibit an excitonic absorption peak at around 2.15 eV for $n = 2$ perovskite and an excitonic absorption peak at around 2.05 eV for $n = 3$ perovskite (Fig. 6c). Furthermore, the PL emission spectra of $n = 3, 4, 5$ thin films are very close, and all the peak positions apparently deviate from their corresponding intrinsic PL emissions determined from the single crystals[83] (Fig. 6d). The full width at half maximum (FWHM) of PL peaks of thin films is also substantially broader than that of exfoliated single crystals. All of this indicates a rise in defects and poor phase purity in thin films.

The multi-phase feature in thin films is further confirmed by ultrafast spectroscopy, based on which the carrier transfer between phases is studied. In $(PEA)_2MA_2Pb_3I_{10}$ ($n = 3$) thin films, four distinct PL peaks corresponding to $n = 2, 3, 4$ and 5 were observed in time-resolved PL measurements once the film was excited. Only PL emission of the smallest bandgap phase remained after about 500 ps.[84] The carriers will transfer from a low n phase to the highest n phase because of the different bandgaps and type-I band alignment, called the energy funnelling effect[85] (Fig. 6e). Along the out-of-plane direction, Zheng *et al.*[86] proposed a distribution model for different phases within the quasi-2D halide perovskite thin films. The phases with lower n values were sandwiched by phases with higher n,
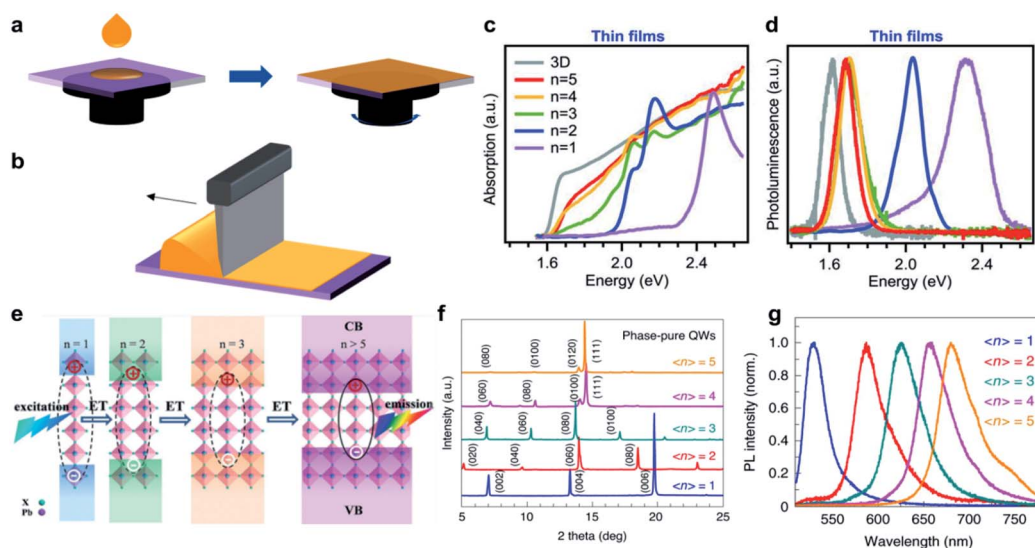

Fig. 6 Quasi-2D perovskite thin film fabrication and their multi-phase nature. Schematics of (a) spin-coating and (b) blade-coating methods. (c) Absorption and (d) PL spectra of $BA_2MA_{n-1}Pb_nI_{3n+1}$ thin films[83] (Copyright: 2017, Science). (e) Illustration of energy funnelling in polycrystalline thin films[85] (Copyright: 2018, Advanced Functional Materials). (f) XRD patterns and (g) normalized PL spectra of $BA_2MA_{n-1}Pb_nI_{3n+1}$ thin films with improved purity[87] (Copyright: 2020, Nature Energy).

This journal is © The Royal Society of Chemistry 2022

J. Mater. Chem. A, 2022, **10**, 19169–19183 | **19175**

facilitating carrier transport in the out-of-plane direction and making charge collection by the corresponding electrodes more efficient.

The above-mentioned energy funnelling effect indicates that the charges could be efficiently transferred between quasi-2D halide perovskites with different n values, highlighting the prospect of using quasi-2D halide perovskite materials as active semiconductors for next-generation optoelectronic devices. However, better phase purity quasi-2D halide perovskite thin films are required in order to gain thorough knowledge of the property–structure relationship. Therefore, plenty of research has been focused on synthesizing thin films with a narrow phase distribution and even pure phase *via* composition or solvent engineering. Liang *et al.*[87] spin-coated a series of BA_2-$MA_{n-1}Pb_nI_{3n+1}$ thin films with different n values. They discovered that thin films with a nearly pure-phase could be achieved by substituting *n*-butylamine acetate (BAAc) for *n*-butylamine iodide (BAI). The XRD patterns of BAAc-based thin films are shown in Fig. 6f. In BAAc-based thin films, clear 2D crystallographic characteristic peaks can be observed, which contrasts sharply with BAI-based thin films. BAI-based thin films with $n >$ 1 have several peaks in their PL spectra, indicating multiple phases with varied n values, while in BAAc-based thin films, nearly single peak emission can be achieved, suggesting improved purity, though the FWHM of PL peaks are sort of broad and there are some shoulders in PL spectra (Fig. 6g).

3.4 Quantum dots

Quantum dots are considered ideal candidates for display technologies due to their tuneable light emission and high PL quantum yield. The synthesis of halide perovskite quantum dots with quantum confinement similar to RP-phase quasi-2D perovskites is mainly implemented *via* one-pot synthesis[88,89] and top-down synthesis.[90,91] In one-pot synthesis, the precursors dissolved in organic solvent are heated and stirred in round-bottom flasks. Oleic acid and oleylamine are commonly used in this method to confine the size of products. Then the products will be centrifuged and redispersed to obtain perovskite quantum dots in solution. By adjusting the molar ratio of precursors, quantum dots with different n values can be achieved. As for top-down synthesis, perovskite quantum dots can be prepared by sonication of as-synthesized bulk single crystals. Compared with bulk crystals, the PL peak of quantum dots will blue-shift sightly because of the size effect, further enlarging the emitting range of quasi-2D perovskites.

3.5 Challenges

With the increase of the n value, the successful synthesis of highly pure quasi-2D halide perovskites becomes increasingly challenging, which is probably related to the crystal growth thermodynamics. Soe *et al.*[46] reported that the formation enthalpy is positive when $n > 5$ in the $BA_2MA_{n-1}Pb_nI_{3n+1}$ series. The components with lower n values are more favored since they are thermodynamically stable. What's more, with higher n values, the difference in formation energy between different quasi-2D halide perovskites becomes minor, making it difficult

to separate the specified phase. In this case, the impact from the kinetics becomes outstanding, like the precise control of crystal growth conditions (mainly supersaturation). To prepare higher n perovskites, a suitable catalyst may be required to lower the activation energy of the desired high n perovskites and alter the reaction pathway.

4. Application

Due to their superior optoelectronic capabilities, outstanding stability, and tunability, quasi-2D halide perovskites are widely employed in light-emitting diodes, solar cells, lasers, photodetectors, and other applications. In this section, we will review the application progress and highlight the challenge of quasi-2D halide perovskites for optoelectronic devices.

4.1 Light-emitting diodes

2D perovskites have high photoluminescence quantum yield (PLQY) and the colour of PL emission can be tuned facilely by altering the composition or n value. As a result, 2D halide perovskites can achieve a wide colour range of light emission[45] (Fig. 7a). Additionally, the relatively narrow FWHM of the emitting peak enables high colour purity. Therefore, 2D halide perovskites are considered the promising candidate for high-performance light-emitting diodes. By integrating red, blue and green LEDs, white electroluminescence (EL) emission can be achieved[92] (Fig. 7b).

Compared with quasi-2D and 3D halide perovskites, pure-2D halide perovskites ($n = 1$) have the strongest quantum confinement and lowest dielectric screening effect. Therefore, nonradiative recombination in pure 2D halide perovskites is lowest because of their large exciton binding energy and short exciton diffusion length. From the perspective of PLQY (Fig. 7c), pure 2D halide perovskites have the top priority in the halide perovskite family.[84] However, when pure-2D halide perovskites are applied as the active layer in a LED, the charge transport will be obstructed at low voltages caused by the large quantity of insulating organic ligands.[93] LEDs based on quasi-2D perovskites are supposed to improve this situation.

An early LED based on quasi-2D perovskites in the visible region was fabricated using $PEA_2MA_{n-1}Pb_nBr_{3n+1}$ ($n = 1$–4), and showed a brightness of 2935 cd m^{-2} and a PLQY of 34%.[93] Yuan *et al.*[84] extended the emission range to the near-infrared region using $PEA_2MA_{n-1}Pb_nI_{3n+1}$ thin films. They compared the performance of devices using quasi-2D perovskites as emissive layers with $n = 3, 5, 10, 40$ and ∞, respectively (Fig. 7d). The device with $n = 5$ showed the highest external quantum efficiency (EQE) of 8.42% on average. As the n value increased, the EQE of devices with $n > 5$ declined. Up to now, the highest EQE of LEDs based on quasi-2D perovskite is 28.1% using $PEA_2Cs_4Pb_5Br_{16}$.[94]

4.2 Solar cells

Halide perovskite is one of the promising candidates for next-generation solar cells. Despite the tremendous progress, numerous obstacles remain, one of which is the poor stability of
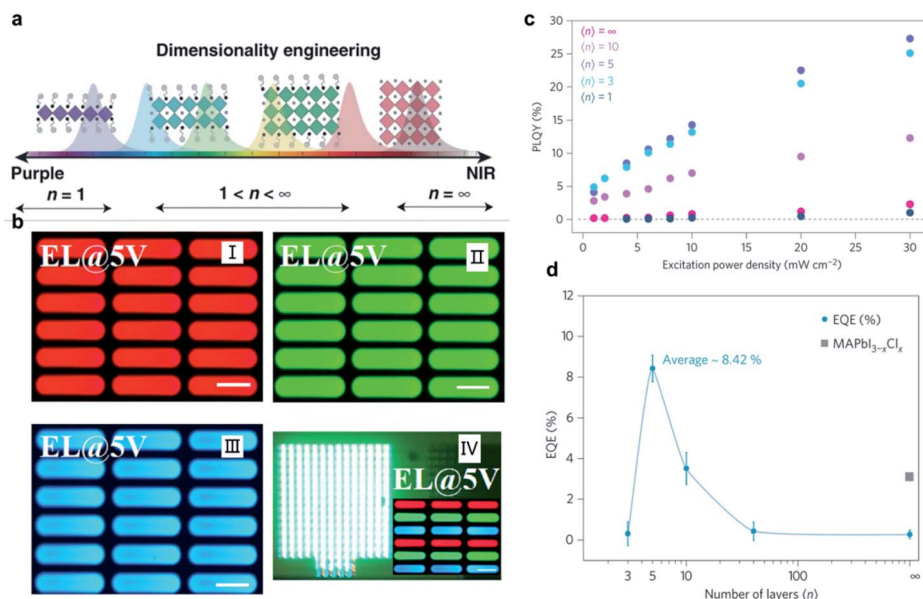
19176 | *J. Mater. Chem. A*, 2022, **10**, 19169–19183

This journal is © The Royal Society of Chemistry 2022

Fig. 7 Colour tunability of quasi-2D perovskites and their application in light-emitting diodes. (a) n-Dependent PL colour tunability[45] (Copyright: 2021, Light: Science & Applications). (b) EL image of RGB monochrome and white quasi-2D perovskite light-emitting diodes (scale bars: 100 μm)[92] (Copyright: 2021, ACS Applied Materials & Interfaces). (c) The relationship between PLQY and excitation power density of $(PEA)_2MA_{n-1}Pb_nI_{3n+1}$ with different n values[86] (Copyright: 2016, Nature Nanotechnology). (d) External quantum efficiency as a function of n value[84] (Copyright: 2016, Nature Nanotechnology).

3D halide perovskites, impeding the commercialization of halide perovskite solar cells.

One proposed solution to this problem is to replace 3D perovskites with quasi-2D perovskites. The metal-halide octahedra in quasi-2D perovskites are better protected from moisture and oxygen by hydrophobic organic ligands. The organic ligands can also diminish metal-halide octahedron distortion and prevent phase transition, owing to their steric hindrance. Another advantage of quasi-2D halide perovskites is the ability to efficiently suppress anionic migration.

Smith $et\ al.$[95] fabricated solar cells based on quasi-2D perovskites for the first time using $(PEA)_2MA_2Pb_3I_{10}$ as the absorption material with a power conversion efficiency (PCE) of 4.73% and open-circuit voltage (V_{OC}) of 1.18 V. These devices showed much lower PCE but higher V_{OC} compared with their 3D perovskite counterparts, which results from higher bandgap originating from the quantum well structure. Quan $et\ al.$[96] fabricated 2D perovskite solar cells based on the $(PEA)_2MA_{n-1}Pb_nI_{3n+1}$ series with n = 1, 2, 3, 6, 10, 40, 60 and ∞. The impact of quantum-well thickness (n value) was studied systematically in their work. As previously stated, the n value here was confirmed by stoichiometry in the precursors. The short-circuit current density (J_{SC}) of devices is shown to increase as n increases, while the V_{OC} decreases (Fig. 8a). This can be attributed to the limited carrier mobility in low-n quasi-2D perovskites, where the influence of organic ligands will strongly hinder the carrier transport. Meanwhile, in quasi-2D perovskites with high n, the strength of the binding energy is relatively weak, resulting in better carrier transport. Low carrier mobility would cause carrier accumulation, leading to high V_{OC} but low J_{SC}. The PCE showed a positive correlation with n

(Fig. 8b). The PCE of those with n > 40 was almost twice that with n = 6. The bandgap of quasi-2D perovskites become narrower with the increase of n. In quasi-2D perovskites with low n, the wide bandgap would lead to insufficient absorption of the solar spectrum especially in the near-infrared range. In a stability test, devices based on 2D perovskites with low n showed less degradation after 1440 hours because of the strong protection from the organic ligands (Fig. 8c). On the other hand, the performance for low n was still lower than for n = 40 due to the poor initial performance.

The performance of the quasi-2D perovskite solar cells is also related to the orientation of the grains. Compared with the in-
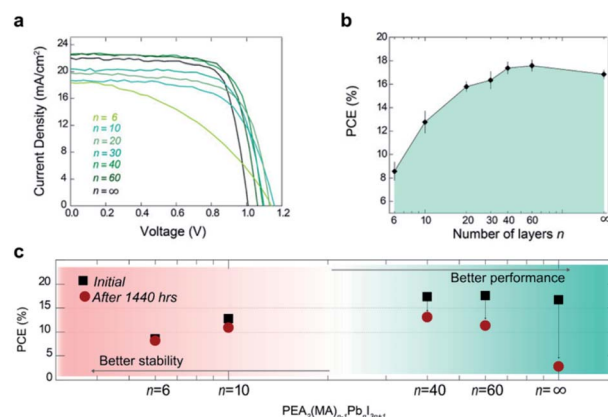

Fig. 8 n-Dependence of quasi-2D halide perovskite solar cell performance. (a) J–V curves of solar cells based on $PEA_2MA_{n-1}Pb_nI_{3n+1}$ (n = 5, 10, 20, 30, 40, 60 and ∞). (b) Power conversion efficiency and (c) stability $versus$ n.[96] (Copyright: 2016, Journal of the American Chemical Society).

plane direction, the conductivity will have a sharp decrease in the out-of-plane direction because of the dielectric organic ligands. In layer-by-layer devices like LEDs and solar cells, this problem will block the carrier transfer in the out-of-plane direction, leading to low performance of devices. One strategy is to alter the crystallographic orientation to make the grains grow vertically. In this way, charge transport and mobility in the out-of-plane direction will be significantly enhanced, resulting in much improved J_{SC} and fill factor.[97] Previous reports showed that the perpendicular heterogeneous nucleation occurring at the liquid–air interface is the origin of vertical orientation.[98] During the crystal growth process, a low supersaturation condition is required to maintain continuous crystal growth along the vertical direction without any other nucleation.[99] In devices fabrication, the adjustment of supersaturation can be achieved by controlling the rate of solvent evaporation, and more specifically, by controlling the additive type[100,101] and quantity,[102] solvent ratio,[103,104] and substrate preheating temperature.[97]

As previously discussed in thin films, there are various co-existing phases with different n values and the proposed energy funnelling effect plays an important role in highly efficient carrier transport, making it difficult to specify the contributions from each phase or other interplay factors such as the energy funnelling effect. In addition, the film-forming conditions have an impact on the dominating n value, therefore the same recipe may correlate with different dominating n values in the final film. To achieve solar cells with near-limit PCE, further understanding of the relationship between the n value and photovoltaic properties is essential. To this end, developing new techniques to precisely control the n value within the quasi-2D halide perovskite thin films is of great significance.

4.3 Laser

In addition to LEDs and solar cells, quasi-2D halide perovskites are also promising gain materials for low-threshold continuous wave lasers.

In quasi-2D perovskite thin films, amplified spontaneous emission (ASE), necessary for lasing, can be observed. It was reported that $(NMA)_2FAPb_2Br_xI_{7-x}$ thin film showed an ultralow ASE threshold less than 20.0 ± 2 μJ cm^{-2}, with outstanding optical stability (more than 32 hours).[85] Using the same organic ligand, room-temperature continuous-wave lasing was achieved by Qin et $al.$[15] Compared with $(PEA)_2FA_7Pb_8Br_{25}$, $(NMA)_2FA_7Pb_8Br_{25}$ thin film showed superior optical stability, which was attributed to the lower triplet exciton energy in the NMA-based perovskite (Fig. 9a). They demonstrated that annihilation of singlet–triplet excitons induced by long-lived triplet excitons reduces the quantity of photons, preventing population inversion. By employing distributed-feedback cavity and triplet management, room-temperature continuous-wave lasing was realized both in PEA-based and NMA-based perovskite thin films. Recent reports indicate that the lasing behaviour in thin films is primarily due to the energy funnelling effect.[13,85,105–108] Zhai et $al.$[108] studied the impact from phase segregation in $PEA_2Cs_2Pb_3Br_{10}$ thin films and found that the lasing phenomenon only happened in the multi-phase region, with a threshold of $\sim$500 μJ cm^{-2}. Apart from thin films, lasing was also observed in quasi-2D perovskite polycrystalline nanowires and rings.[12,38]

As opposed to multi-phase materials, lasing is also observed in pure-phase single crystals. Recent discoveries suggest that quasi-2D perovskite single crystals are a superior alternative to elucidate the fundamental physical mechanisms and realize ultralow threshold lasers. Raghavan et $al.$[63] reported millimetre-sized $(BA)_2(MA)_{n-1}Pb_nI_{3n+1}$ ($n = 1, 2, 3$) single crystals with
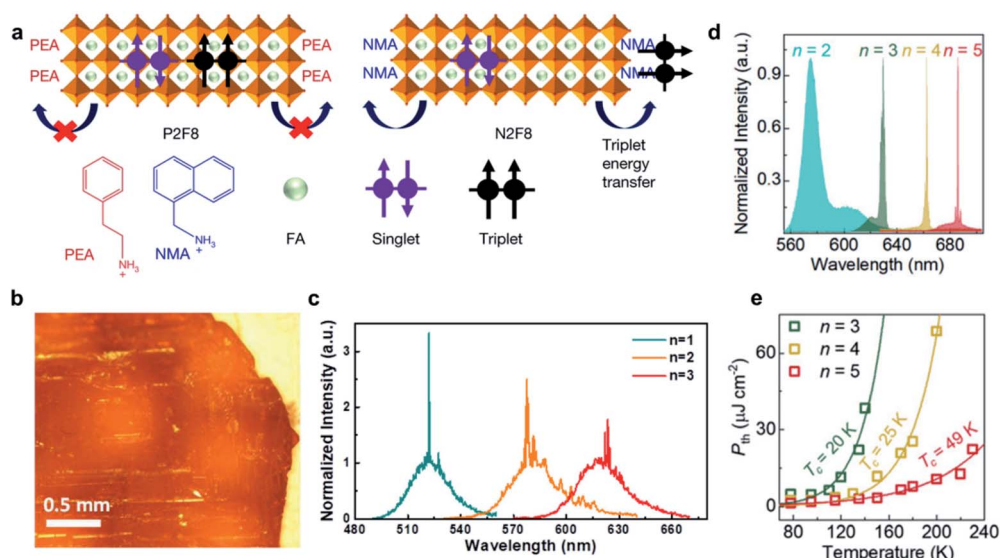

Fig. 9 Lasers based on quasi-2D halide perovskites. (a) Chemical structure and triplet energy transport of PEA–based and NMA–based quasi-2D perovskites[15] (Copyright: 2020, Nature). (b) The bottom surface of a millimetre-sized $(BA)_2PbI_4$ single crystal[63] (Copyright: 2018, Nano Letters). (c) Lasing with different wavelengths in $(BA)_2(MA)_{n-1}Pb_nI_{3n+1}$ quasi-2D perovskites[63] (Copyright: 2018, Nano Letters). (d) Lasing spectra of exfoliated $(BA)_2(MA)_{n-1}Pb_nI_{3n+1}$ single crystals at 77 K (ref. 109) (Copyright: 2019, Advanced Materials). (e) Temperature dependence of lasing thresholds of exfoliated $(BA)_2(MA)_{n-1}Pb_nI_{3n+1}$ single crystals[109] (Copyright: 2019, Advanced Materials).

19178 | *J. Mater. Chem. A*, 2022, **10**, 19169–19183

This journal is © The Royal Society of Chemistry 2022

a quite low lasing threshold ranging from 2.85 to 3.21 μJ cm^{-2} (Fig. 9b and c). Such low lasing thresholds result from the stepped-pyramidal morphology and the large refractive index difference between air and perovskite.

Subsequently, to explore the quasi-2D perovskites' applications in low-power consumption and chip-level coherent light sources for optoelectronic applications and better understand the microlasing in homologous quasi-2D perovskites, Liang et al.[109] studied the ASE and lasing behaviours of mechanically exfoliated $(BA)_2(MA)_{n-1}Pb_nI_{3n+1}$ thin crystals. Unlike the situation in uniform bulk single-crystals discussed above, the ASE phenomenon was only observed in the perovskites with $n = 3$, 4 and 5 (Fig. 9d). As shown in Fig. 9e, the increase of the n value resulted in the decrease of the lasing threshold, both in pump laser intensity and temperature. The underlying mechanism of this trend may lie in the enhanced Auger recombination and stronger exciton–phonon interaction in the lower n phase, which extensively constrained the optical gain in 2D perovskites.

According to the discussion above, high-n value and high-quality quasi-2D perovskite single crystals exhibit huge potential as a candidate for highly stable lasers with ultralow threshold and ultra-narrow lasing FWHM.

4.4 Photodetectors

Quasi-2D perovskites also show fascinating performance in photodetectors with high photoresponsivity, detectivity and response rate. To fabricate high-performance photodetectors, the coexistence of high responsivity, detectivity and response rate is essential. However, there is a dilemma that high photocurrent necessitates highly crystalline materials with effective conductivity, but dark current suppression necessitates a large number of defects to prevent thermally excited carriers from being transported.

To confront this challenge, Feng et al.[16] took advantage of the anisotropy and unique low-energy edge states of quasi-2D perovskites to selectively suppress the dark current. They fabricated nanowire-based photodetectors (Fig. 10a) using $BA_2MA_{n-1}Pb_nI_{3n+1}$ ($n = 2$–5), and controlled the crystal orientation to make the wire length perpendicular to the perovskite layers and the spatially confined height and width parallel to the perovskite layer. Under illumination, the tightly bound excitons generated at the bulk nanowires will transfer to and dissociate efficiently in trace amounts of exposed layer edges, enabling photocarriers to be generated at the bulk nanowires but conduct at the edges. Furthermore, as a result of the unidirectional flow from the bulk to the surface, the photocarriers will directly establish contact with the top-contact electrodes (Fig. 10b). In this way, it is possible to achieve both a high resistance for dark current suppression and a high-photoconductivity channel. In addition, the impact of the n value on photodetector performance was examined in their research. From $n = 2$ to $n = 4$, the dark currents show a slight increase while the photocurrents significantly improve (Fig. 10c and d). Compared with quasi-2D crystals ($n = 2$), the superior photocurrent and responsivity of the higher n perovskite photodetector may originate from efficient exciton dissociation, carrier conduction and charge injection at crystallite edges. The best-performing devices ($n = 4$) show high responsivities of 1.5 $\times$ 10^4 A W^{-1}, detectivities of 7 $\times$ 10^{15} Jones and response time of 25 μs. The slight drop of performance in $n = 5$ devices compared with $n = 4$ devices may be caused by less suppression of dark current from fewer organic barriers and higher defect density.

Fig. 10 Photodetectors based on quasi-2D halide perovskites. (a) Device structure of quasi-2D photodetectors based on single crystalline nanowire arrays. (b) Carrier dynamics in quasi-2D photodetectors based on single crystalline nanowire arrays. The I–V curves of $(BA)_2(MA)_{n-1}Pb_nI_{3n+1}$ quasi-2D perovskites in (c) the dark state and under (d) light illumination[16] (Copyright: 2018, Nature Electronics). (e) Photocurrent and (f) responsivity versus voltage[55] (Copyright: 2018, ACS Nano).

Meanwhile, the same *n*-dependent performance can be seen in photodetectors with exfoliated crystals (Fig. 10e and f), which also show ultrasensitive detectivity.[17,55,73]

5. Conclusions and perspectives

In summary, pure-2D perovskites possess better stability, and larger exciton binding energy and bandgap, while 3D perovskites possess higher carrier mobility, longer carrier lifetime and smaller bandgap. From the perspective of crystal structure, quasi-2D halide perovskites can be viewed as the heterostructures stacked by repeated pure-2D and 3D halide perovskites. Compared with their pure-2D and 3D counterparts, quasi-2D perovskites provide a compromise in properties and a possibility for diverse high-performance applications (such as LEDs, solar cells, *etc.*) and could potentially integrate the merits from both pure-2D and 3D halide perovskites.

On the other hand, from the perspective of materials science, the biggest challenge for the quasi-2D halide perovskite area is how to precisely control the *n* value in the single-crystal or polycrystalline material forms, and how to establish the relationship between the optoelectronic/electronic/ferroelectric properties and the specific structural parameters, such as *n* value, A-site cations and L-site organic ligands, *etc.* Because of the growth thermodynamics, the synthesis of high *n* 2D perovskites with high phase purity is quite tricky and challenging. In addition, tin (Sn)-based perovskites possess a smaller bandgap and higher carrier mobility compared with their Pb-based counterparts. However, in Sn-based perovskites, the Sn^{2+} will be easily oxidized into Sn^{4+}, causing the destruction of perovskite structure and degradation of corresponding devices, which causes difficulties in the fundamental and application studies of Sn-based quasi-2D halide perovskites.

Based on the current research progress, we propose the following synthetic strategies for achieving high-purity quasi-2D Pb-based and Sn-based halide perovskite crystals:

1. Composition engineering *via* organic ligand selection and incorporation. Previous efforts suggest that the ligands will affect the preferred distribution of *n* value. Conjugated organic ligands with strong van der Waals interaction with their organic neighbours may be helpful to stabilize higher *n* structure. In addition, as the bulky organic ligands can improve the environmental stability of halide perovskites and suppress the anionic migration, the high-throughput selection and incorporation of appropriate bulky organic ligands into quasi-2D halide perovskite lattices may bring new opportunities to control the *n* value and stabilize sensitive perovskites such as Sn-based quasi-2D halide perovskites.

2. Mechanochemistry. In mechanochemistry, the reaction energy is provided by mechanical force. This method can avoid the use of solvent and provide a relatively pure reaction environment. Compared with the solution method, effects from solvent can be avoided, hence providing a possible approach to synthesize high-*n* quasi-2D halide perovskites with high phase purity.

3. Catalysts. Though *n* > 5 quasi-2D perovskites are not as thermodynamically stable as pure-2D and *n* < 5 quasi-2D perovskites, effective catalysts may alter the dynamic process, allowing highly selective synthesis and precise control of the *n* value.

Based on the excellent properties and unique structure of high-purity quasi-2D halide perovskites, additional applications could be envisioned beyond the optoelectronic applications discussed above. For example, the non-centrosymmetry induced by the organic ligands in pure-2D and quasi-2D halide perovskites will lead to the in-plane ferroelectricity within these materials. And there is discussion and assumption that the dipoles inside the halide perovskites brought by ferroelectrics could make the carrier separation more efficient, which might be one of the physical origins to justify the excellent photovoltaic performance of halide perovskite solar cells.[110-116] Thus, a great variety of quasi-2D halide perovskites with tunable band structures provide a material platform to study the photovoltaic–ferroelectric correlation. Based on this, solar cells with higher efficiency might be achieved. In addition, as discussed above, Sn-based halide perovskites have lower bandgap and higher carrier mobility. Developing a high-purity quasi-2D halide perovskite with different *n* values and improved stability will provide more materials as candidates to develop high-performance Sn-based perovskite transistors and even ferroelectric transistors.

Conflicts of interest

There are no conflicts to declare.

Notes and references

1 M. Shao, T. Bie, L. Yang, Y. Gao, X. Jin, F. He, N. Zheng, Y. Yu and X. Zhang, *Adv. Mater.*, 2022, **34**, 2107211.

2 J. Liang, Z. Zhang, Q. Xue, Y. Zheng, X. Wu, Y. Huang, X. Wang, C. Qin, Z. Chen and C.-C. Chen, *Energy Environ. Sci.*, 2022, **15**, 296–310.

3 W. Li, S. Sidhik, B. Traore, R. Asadpour, J. Hou, H. Zhang, A. Fehr, J. Essman, Y. Wang, J. M. Hoffman, I. Spanopoulos, J. J. Crochet, E. Tsai, J. Strzalka, C. Katan, M. A. Alam, M. G. Kanatzidis, J. Even, J. C. Blancon and A. D. Mohite, *Nat. Nanotechnol.*, 2022, **17**, 45–52.

4 X. Li, K. Li, B. X. Wang, X. N. Zhang, S. L. Yue, Y. X. Li, Q. Chen, S. L. Li, T. Yue, H. Q. Zhou and Y. Zhang, *Adv. Funct. Mater.*, 2021, **31**, 2107675.

5 Y. Zhang and N.-G. Park, *ACS Energy Lett.*, 2022, **7**, 757–765.

6 P. Pang, G. Jin, C. Liang, B. Wang, W. Xiang, D. Zhang, J. Xu, W. Hong, Z. Xiao, L. Wang, G. Xing, J. Chen and D. Ma, *ACS Nano*, 2020, **14**, 11420–11430.

7 H. Chen, J. Lin, J. Kang, Q. Kong, D. Lu, J. Kang, M. Lai, L. N. Quan, Z. Lin, J. Jin, L. W. Wang, M. F. Toney and P. Yang, *Sci. Adv.*, 2020, **6**, eaay4045.

8 F. Yuan, X. Zheng, A. Johnston, Y. K. Wang, C. Zhou, Y. Dong, B. Chen, H. Chen, J. Z. Fan, G. Sharma, P. Li, Y. Gao, O. Voznyy, H. T. Kung, Z. H. Lu, O. M. Bakr and E. H. Sargent, *Sci. Adv.*, 2020, **6**, eabb0253.

9 Y. Liu, L. Zhang, S. Chen, C. Liu, Y. Li, J. Wu, D. Wang, Z. Jiang, Y. Li, Y. Li, X. Wang and B. Xu, *Small*, 2021, **17**, 2101477.

19180 | *J. Mater. Chem. A*, 2022, **10**, 19169–19183

This journal is © The Royal Society of Chemistry 2022

10 Z. Guo, Y. Zhang, B. Wang, L. Wang, N. Zhou, Z. Qiu, N. Li, Y. Chen, C. Zhu, H. Xie, T. Song, L. Song, H. Xue, S. Tao, Q. Chen, G. Xing, L. Xiao, Z. Liu and H. Zhou, *Adv. Mater.*, 2021, **33**, 2102246.

11 A. D. Jodlowski, A. Yepez, R. Luque, L. Camacho and G. de Miguel, *Angew. Chem., Int. Ed.*, 2016, **55**, 14972–14977.

12 H. Zhang, Q. Liao, Y. Wu, Z. Zhang, Q. Gao, P. Liu, M. Li, J. Yao and H. Fu, *Adv. Mater.*, 2018, **30**, 1706186.

13 M. R. Leyden, S. Terakawa, T. Matsushima, S. B. Ruan, K. Goushi, M. Auffray, A. S. D. Sandanayaka, C. J. Qin, F. Bencheikh and C. Adachi, *ACS Photonics*, 2019, **6**, 460–466.

14 C. H. Lin, B. Cheng, T. Y. Li, J. R. D. Retamal, T. C. Wei, H. C. Fu, X. Fang and J. H. He, *ACS Nano*, 2019, **13**, 1168–1176.

15 C. Qin, A. S. D. Sandanayaka, C. Zhao, T. Matsushima, D. Zhang, T. Fujihara and C. Adachi, *Nature*, 2020, **585**, 53–57.

16 J. G. Feng, C. Gong, H. F. Gao, W. Wen, Y. J. Gong, X. Y. Jiang, B. Zhang, Y. C. Wu, Y. S. Wu, H. B. Fu, L. Jiang and X. Zhang, *Nat. Electron.*, 2018, **1**, 404–410.

17 K. Leng, I. Abdelwahab, I. Verzhbitskiy, M. Telychko, L. Chu, W. Fu, X. Chi, N. Guo, Z. Chen, Z. Chen, C. Zhang, Q. H. Xu, J. Lu, M. Chhowalla, G. Eda and K. P. Loh, *Nat. Mater.*, 2018, **17**, 908–914.

18 Y. C. Liu, H. C. Ye, Y. X. Zhang, K. Zhao, Z. Yang, Y. B. Yuan, H. D. Wu, G. T. Zhao, Z. P. Yang, J. Tang, Z. Xu and S. Z. Liu, *Matter*, 2019, **1**, 465–480.

19 T. Ji, H. K. Zhang, N. Han, W. Y. Wang, B. Wu, G. H. Li, M. M. Fan, Z. F. Li, Y. Y. Hao, F. R. Zhu, Y. C. Wu and Y. X. Cui, *J. Mater. Chem. C*, 2020, **8**, 1110–1117.

20 S. Wang, Y. Chen, J. J. Yao, G. X. Zhao, L. Z. Li and G. F. Zou, *J. Mater. Chem. C*, 2021, **9**, 6498–6506.

21 C. Katan, N. Mercier and J. Even, *Chem. Rev.*, 2019, **119**, 3140–3192.

22 X. Han, Y. S. Zheng, S. D. Chai, S. H. Chen and J. L. Xu, *Nanophotonics*, 2020, **9**, 1787–1810.

23 Y. K. Xu, M. Wang, Y. T. Lei, Z. P. Ci and Z. W. Jin, *Adv. Energy Mater.*, 2020, **10**, 2002558.

24 L. L. Gao, J. X. You and S. Z. Liu, *J. Energy Chem.*, 2021, **57**, 69–82.

25 Y. S. Lei, Y. M. Chen and S. Xu, *Matter*, 2021, **4**, 2266–2308.

26 S. N. Ruddlesden and P. Popper, *Acta Crystallogr*, 1958, **11**, 54–55.

27 M. Dion, M. Ganne and M. Tournoux, *Mater. Res. Bull.*, 1981, **16**, 1429–1435.

28 A. J. Jacobson, J. W. Johnson and J. T. Lewandowski, *Inorg. Chem.*, 2002, **24**, 3727–3729.

29 C. M. M. Soe, C. C. Stoumpos, M. Kepenekian, B. Traore, H. Tsai, W. Nie, B. Wang, C. Katan, R. Seshadri, A. D. Mohite, J. Even, T. J. Marks and M. G. Kanatzidis, *J. Am. Chem. Soc.*, 2017, **139**, 16297–16309.

30 N. Mercier, *Angew. Chem., Int. Ed.*, 2019, **58**, 17912–17917.

31 M. C. Weidman, M. Seitz, S. D. Stranks and W. A. Tisdale, *ACS Nano*, 2016, **10**, 7830–7839.

32 Z. Wang, Z. Lu, Z. Xu, J. Hu, Y. Chen, C. Zhang, Y. Wang, F. Guo and Y. Mai, *Adv. Sci.*, 2021, **8**, e2101856.

33 J. Zhang and B. Hu, *Nano Energy*, 2020, **76**, 104999.

34 F. Wang, Z. Wang, W. Sun, Z. Wang, Y. Bai, T. Hayat, A. Alsaedi and Z. Tan, *Small*, 2020, **16**, 2002940.

35 Y. Jin, Z. K. Wang, S. Yuan, Q. Wang, C. Qin, K. L. Wang, C. Dong, M. Li, Y. Liu and L. S. Liao, *Adv. Funct. Mater.*, 2019, **30**, 1908339.

36 Y. Yang, S. Xu, Z. Ni, C. H. Van Brackle, L. Zhao, X. Xiao, X. Dai and J. Huang, *Adv. Mater.*, 2021, **33**, 2100783.

37 H. D. Lee, H. Kim, H. Cho, W. Cha, Y. Hong, Y. H. Kim, A. Sadhanala, V. Venugopalan, J. S. Kim, J. W. Choi, C. L. Lee, D. Kim, H. Yang, R. H. Friend and T. W. Lee, *Adv. Funct. Mater.*, 2019, **29**, 1901225.

38 H. Zhang, Y. Wu, Q. Liao, Z. Zhang, Y. Liu, Q. Gao, P. Liu, M. Li, J. Yao and H. Fu, *Angew. Chem., Int. Ed.*, 2018, **57**, 7748–7752.

39 Y. Gao, E. Shi, S. Deng, S. B. Shiring, J. M. Snaider, C. Liang, B. Yuan, R. Song, S. M. Janke, A. Liebman-Pelaez, P. Yoo, M. Zeller, B. W. Boudouris, P. Liao, C. Zhu, V. Blum, Y. Yu, B. M. Savoie, L. Huang and L. Dou, *Nat. Chem.*, 2019, **11**, 1151–1157.

40 S. Silver, Q. Dai, H. Li, J. L. Brédas and A. Kahn, *Adv. Energy Mater.*, 2019, **9**, 1901005.

41 J. A. Sichert, Y. Tong, N. Mutz, M. Vollmer, S. Fischer, K. Z. Milowska, R. Garcia Cortadella, B. Nickel, C. Cardenas-Daw, J. K. Stolarczyk, A. S. Urban and J. Feldmann, *Nano Lett.*, 2015, **15**, 6521–6527.

42 L. Polavarapu, B. Nickel, J. Feldmann and A. S. Urban, *Adv. Energy Mater.*, 2017, **7**, 1700267.

43 J. Even, L. Pedesseau and C. Katan, *ChemPhysChem*, 2014, **15**, 3733–3741.

44 R. Chakraborty and A. Nag, *Phys. Chem. Chem. Phys.*, 2021, **23**, 82–93.

45 L. Zhang, C. Sun, T. He, Y. Jiang, J. Wei, Y. Huang and M. Yuan, *Light. Sci. Appl.*, 2021, **10**, 61.

46 C. M. M. Soe, G. P. Nagabhushana, R. Shivaramaiah, H. Tsai, W. Nie, J. C. Blancon, F. Melkonyan, D. H. Cao, B. Traore, L. Pedesseau, M. Kepenekian, C. Katan, J. Even, T. J. Marks, A. Navrotsky, A. D. Mohite, C. C. Stoumpos and M. G. Kanatzidis, *Proc. Natl. Acad. Sci. U. S. A.*, 2019, **116**, 58–66.

47 J. Tauc, R. Grigorovici and A. Vancu, *Phys. Status Solidi B*, 1966, **15**, 627–637.

48 S. Deng, E. Shi, L. Yuan, L. Jin, L. Dou and L. Huang, *Nat. Commun.*, 2020, **11**, 664.

49 W. Chen, Y. Shi, J. Chen, P. Ma, Z. Fang, D. Ye, Y. Lu, Y. Yuan, J. Zhao and Z. Xiao, *Adv. Mater.*, 2021, **33**, 2104842.

50 Z. Guo, X. Wu, T. Zhu, X. Zhu and L. Huang, *ACS Nano*, 2016, **10**, 9992–9998.

51 S. Wang, J. Ma, W. Li, J. Wang, H. Wang, H. Shen, J. Li, J. Wang, H. Luo and D. Li, *J. Phys. Chem. Lett.*, 2019, **10**, 2546–2553.

52 D. Ghosh, A. J. Neukirch and S. Tretiak, *J. Phys. Chem. Lett.*, 2020, **11**, 2955–2964.

53 Y. Shao, W. Gao, H. Yan, R. Li, I. Abdelwahab, X. Chi, L. Rogee, L. Zhuang, W. Fu, S. P. Lau, S. F. Yu, Y. Cai, K. P. Loh and K. Leng, *Nat. Commun.*, 2022, **13**, 138.

This journal is © The Royal Society of Chemistry 2022

J. Mater. Chem. A, 2022, **10**, 19169–19183 | **19181**

54 A. Chernikov, T. C. Berkelbach, H. M. Hill, A. Rigosi, Y. Li, O. B. Aslan, D. R. Reichman, M. S. Hybertsen and T. F. Heinz, *Phys. Rev. Lett.*, 2014, **113**, 076802.

55 K. Wang, C. Wu, D. Yang, Y. Jiang and S. Priya, *ACS Nano*, 2018, **12**, 4919–4929.

56 Akriti, E. Shi, S. B. Shiring, J. Yang, C. L. Atencio-Martinez, B. Yuan, X. Hu, Y. Gao, B. P. Finkenauer, A. J. Pistone, Y. Yu, P. Liao, B. M. Savoie and L. Dou, *Nat. Nanotechnol.*, 2021, **16**, 584–591.

57 Akriti, S. Zhang, Z. Y. Lin, E. Shi, B. P. Finkenauer, Y. Gao, A. J. Pistone, K. Ma, B. M. Savoie and L. Dou, *Adv. Mater.*, 2021, **33**, 2105183.

58 C. C. Stoumpos, D. H. Cao, D. J. Clark, J. Young, J. M. Rondinelli, J. I. Jang, J. T. Hupp and M. G. Kanatzidis, *Chem. Mater.*, 2016, **28**, 2852–2867.

59 C. C. Stoumpos, C. M. M. Soe, H. Tsai, W. Nie, J.-C. Blancon, D. H. Cao, F. Liu, B. Traoré, C. Katan, J. Even, A. D. Mohite and M. G. Kanatzidis, *Chem*, 2017, **2**, 427–440.

60 L. Mao, R. M. Kennard, B. Traore, W. Ke, C. Katan, J. Even, M. L. Chabinyc, C. C. Stoumpos and M. G. Kanatzidis, *Chem*, 2019, **5**, 2593–2604.

61 J. Wang, Y. Mi, X. Gao, J. Li, J. Li, S. Lan, C. Fang, H. Shen, X. Wen, R. Chen, X. Liu, T. He and D. Li, *Adv. Opt. Mater.*, 2019, **7**, 1900398.

62 X. T. Li, Y. P. Fu, L. Pedesseau, P. J. Guo, S. Cuthriell, I. Hadar, J. Even, C. Katan, C. C. Stoumpos, R. D. Schaller, E. Harel and M. G. Kanatzidis, *J. Am. Chem. Soc.*, 2020, **142**, 11486–11496.

63 C. M. Raghavan, T. P. Chen, S. S. Li, W. L. Chen, C. Y. Lo, Y. M. Liao, G. Haider, C. C. Lin, C. C. Chen, R. Sankar, Y. M. Chang, F. C. Chou and C. W. Chen, *Nano Lett.*, 2018, **18**, 3221–3228.

64 X. Xiao, J. Dai, Y. Fang, J. Zhao, X. Zheng, S. Tang, P. N. Rudd, X. C. Zeng and J. Huang, *ACS Energy Lett.*, 2018, **3**, 684–688.

65 W. Paritmongkol, N. S. Dahod, A. Stollmann, N. N. Mao, C. Settens, S. L. Zheng and W. A. Tisdale, *Chem. Mater.*, 2019, **31**, 5592–5607.

66 J. Li, J. Wang, Y. Zhang, H. Wang, G. Lin, X. Xiong, W. Zhou, H. Luo and D. Li, *2D Mater.*, 2018, **5**, 021001.

67 S. Han, P. Wang, J. Zhang, X. Liu, Z. Sun, X. Huang, L. Li, C. Ji, W. Zhang, B. Teng, W. Hu, M. Hong and J. Luo, *Laser Photonics Rev.*, 2018, **12**, 1800060.

68 M. Cinquino, L. Polimeno, G. Lerario, M. De Giorgi, A. Moliterni, V. Olieric, A. Fieramosca, S. Carallo, R. Mastria, V. Ardizzone, L. Dominici, D. Ballarini, C. Giannini, D. Sanvitto, A. Rizzo and L. De Marco, *J. Lumin.*, 2020, **221**, 117079.

69 M. Cinquino, A. Fieramosca, R. Mastria, L. Polimeno, A. Moliterni, V. Olieric, N. Matsugaki, R. Panico, M. De Giorgi, G. Gigli, C. Giannini, A. Rizzo, D. Sanvitto and L. De Marco, *Adv. Mater.*, 2021, **33**, 2102326.

70 J. Wang, J. Li, Q. Tan, L. Li, J. Zhang, J. Zang, P. Tan, J. Zhang and D. Li, *J. Phys. Chem. Lett.*, 2017, **8**, 6211–6219.

71 W. Peng, J. Yin, K. T. Ho, O. Ouellette, M. De Bastiani, B. Murali, O. El Tall, C. Shen, X. Miao, J. Pan, E. Alarousu,

J. H. He, B. S. Ooi, O. F. Mohammed, E. Sargent and O. M. Bakr, *Nano Lett.*, 2017, **17**, 4759–4767.

72 G. Liu, J. Liu, Z. Fan, X. He, K. Luo, Q. Ye and C. Liao, *Phys. Status Solidi RRL*, 2021, **15**, 2100099.

73 L. Li, Z. Sun, P. Wang, W. Hu, S. Wang, C. Ji, M. Hong and J. Luo, *Angew. Chem., Int. Ed.*, 2017, **56**, 12150–12154.

74 L. Li, X. Shang, S. Wang, N. Dong, C. Ji, X. Chen, S. Zhao, J. Wang, Z. Sun, M. Hong and J. Luo, *J. Am. Chem. Soc.*, 2018, **140**, 6806–6809.

75 E. S. Vasileiadou, I. Hadar, M. Kepenekian, J. Even, Q. Tu, C. D. Malliakas, D. Friedrich, I. Spanopoulos, J. M. Hoffman, V. P. Dravid and M. G. Kanatzidis, *Chem. Mater.*, 2021, **33**, 5085–5107.

76 C. Ji, Y. Li, X. Liu, Y. Wang, T. Zhu, Q. Chen, L. Li, S. Wang and J. Luo, *Angew. Chem., Int. Ed. Engl.*, 2021, **60**, 20970–20976.

77 N. Mercier, *CrystEngComm*, 2005, **7**, 429–432.

78 L. Dou, A. B. Wong, Y. Yu, M. Lai, N. Kornienko, S. W. Eaton, A. Fu, C. G. Bischak, J. Ma, T. Ding, N. S. Ginsberg, L. W. Wang, A. P. Alivisatos and P. Yang, *Science*, 2015, **349**, 1518–1521.

79 E. Shi, B. Yuan, S. B. Shiring, Y. Gao, Akriti, Y. Guo, C. Su, M. Lai, P. Yang, J. Kong, B. M. Savoie, Y. Yu and L. Dou, *Nature*, 2020, **580**, 614–620.

80 D. Pan, Y. Fu, N. Spitha, Y. Zhao, C. R. Roy, D. J. Morrow, D. D. Kohler, J. C. Wright and S. Jin, *Nat. Nanotechnol.*, 2021, **16**, 159–165.

81 R. Guo, Z. Zhu, A. Boulesbaa, F. Hao, A. Puretzky, K. Xiao, J. Bao, Y. Yao and W. Li, *Small Methods*, 2017, **1**, 1700245.

82 J. Chen, Y. Wang, L. Gan, Y. He, H. Li and T. Zhai, *Angew. Chem., Int. Ed.*, 2017, **56**, 14893–14897.

83 J. C. Blancon, H. Tsai, W. Nie, C. C. Stoumpos, L. Pedesseau, C. Katan, M. Kepenekian, C. M. Soe, K. Appavoo, M. Y. Sfeir, S. Tretiak, P. M. Ajayan, M. G. Kanatzidis, J. Even, J. J. Crochet and A. D. Mohite, *Science*, 2017, **355**, 1288–1292.

84 M. Yuan, L. N. Quan, R. Comin, G. Walters, R. Sabatini, O. Voznyy, S. Hoogland, Y. Zhao, E. M. Beauregard, P. Kanjanaboos, Z. Lu, D. H. Kim and E. H. Sargent, *Nat. Nanotechnol.*, 2016, **11**, 872–877.

85 M. L. Li, Q. G. Gao, P. Liu, Q. Liao, H. H. Zhang, J. N. Yao, W. P. Hu, Y. S. Wu and H. B. Fu, *Adv. Funct. Mater.*, 2018, **28**, 1707006.

86 F. Zheng, C. R. Hall, D. Angmo, C. Zuo, S. Rubanov, Z. Wen, S. J. Bradley, X.-T. Hao, M. Gao, T. A. Smith and K. P. Ghiggino, *J. Mater. Chem. C*, 2021, **9**, 5362–5372.

87 C. Liang, H. Gu, Y. Xia, Z. Wang, X. Liu, J. Xia, S. Zuo, Y. Hu, X. Gao, W. Hui, L. Chao, T. Niu, M. Fang, H. Lu, H. Dong, H. Yu, S. Chen, X. Ran, L. Song, B. Li, J. Zhang, Y. Peng, G. Shao, J. Wang, Y. Chen, G. Xing and W. Huang, *Nat. Energy*, 2020, **6**, 38–45.

88 Q. A. Akkerman, S. G. Motti, A. R. Srimath Kandada, E. Mosconi, V. D'Innocenzo, G. Bertoni, S. Marras, B. A. Kamino, L. Miranda, F. De Angelis, A. Petrozza, M. Prato and L. Manna, *J. Am. Chem. Soc.*, 2016, **138**, 1010–1016.

89 Y. H. Chang, J. C. Lin, Y. C. Chen, T. R. Kuo and D. Y. Wang, *Nanoscale Res. Lett.*, 2018, **13**, 247.

90 S. J. Varma, J. Cherusseri, J. Li, J. Kumar, E. Barrios and J. Thomas, *AIP Adv.*, 2020, **10**, 045130.

91 J. Zhao, Z. Zheng, W. Liu, X. Tang, D. Jin and X. Wang, *J. Mater. Sci.: Mater. Electron.*, 2020, **32**, 12922–12928.

92 J. Wang, D. Li, L. Mu, M. Li, Y. Luo, B. Zhang, C. Mai, B. Guo, L. Lan, J. Wang, H. L. Yip and J. Peng, *ACS Appl. Mater. Interfaces*, 2021, **13**, 41773–41781.

93 J. Byun, H. Cho, C. Wolf, M. Jang, A. Sadhanala, R. H. Friend, H. Yang and T.-W. Lee, *Adv. Mater.*, 2016, **28**, 7515–7520.

94 Z. Liu, W. Qiu, X. Peng, G. Sun, X. Liu, D. Liu, Z. Li, F. He, C. Shen, Q. Gu, F. Ma, H.-L. Yip, L. Hou, Z. Qi and S.-J. Su, *Adv. Mater.*, 2021, **33**, 2103268.

95 I. C. Smith, E. T. Hoke, D. Solis-Ibarra, M. D. McGehee and H. I. Karunadasa, *Angew. Chem., Int. Ed.*, 2014, **53**, 11232–11235.

96 L. N. Quan, M. Yuan, R. Comin, O. Voznyy, E. M. Beauregard, S. Hoogland, A. Buin, A. R. Kirmani, K. Zhao, A. Amassian, D. H. Kim and E. H. Sargent, *J. Am. Chem. Soc.*, 2016, **138**, 2649–2655.

97 H. Tsai, W. Nie, J. C. Blancon, C. C. Stoumpos, R. Asadpour, B. Harutyunyan, A. J. Neukirch, R. Verduzco, J. J. Crochet, S. Tretiak, L. Pedesseau, J. Even, M. A. Alam, G. Gupta, J. Lou, P. M. Ajayan, M. J. Bedzyk and M. G. Kanatzidis, *Nature*, 2016, **536**, 312–316.

98 A. Z. Chen, M. Shiu, J. H. Ma, M. R. Alpert, D. Zhang, B. J. Foley, D. M. Smilgies, S. H. Lee and J. J. Choi, *Nat. Commun.*, 2018, **9**, 1336.

99 A. Z. Chen, M. Shiu, X. Deng, M. Mahmoud, D. Zhang, B. J. Foley, S.-H. Lee, G. Giri and J. J. Choi, *Chem. Mater.*, 2019, **31**, 1336–1343.

100 X. Zhang, G. Wu, W. Fu, M. Qin, W. Yang, J. Yan, Z. Zhang, X. Lu and H. Chen, *Adv. Energy Mater.*, 2018, **8**, 1702498.

101 C. Lan, G. Liang, S. Zhao, B. Fan, H. Lan, H. Peng, H. Sun, D. Zhang, J. Luo and P. Fan, *J. Am. Chem. Soc.*, 2019, **102**, 4152–4160.

102 X. Zhang, G. Wu, S. Yang, W. Fu, Z. Zhang, C. Chen, W. Liu, J. Yan, W. Yang and H. Chen, *Small*, 2017, **13**, 1700611.

103 L. Gao, F. Zhang, C. Xiao, X. Chen, B. W. Larson, J. J. Berry and K. Zhu, *Adv. Funct. Mater.*, 2019, **29**, 1901652.

104 A. Caiazzo, K. Datta, J. Jiang, M. C. Gelvez-Rueda, J. Li, R. Ollearo, J. M. Vicent-Luna, S. Tao, F. C. Grozema, M. M. Wienk and R. A. J. Janssen, *Adv. Energy Mater.*, 2021, **11**, 2102144.

105 M. Cui, C. Qin, Y. Jiang, M. Yuan, L. Xu, D. Song, Y. Jiang and Y. Liu, *J. Phys. Chem. Lett.*, 2020, **11**, 5734–5740.

106 L. Lei, D. Seyitliyev, S. Stuard, J. Mendes, Q. Dong, X. Fu, Y.-A. Chen, S. He, X. Yi, L. Zhu, C.-H. Chang, H. Ade, K. Gundogdu and F. So, *Adv. Mater.*, 2020, **32**, 1906571.

107 M. R. Leyden, T. Matsushima, C. Qin, S. Ruan, H. Ye and C. Adachi, *Phys. Chem. Chem. Phys.*, 2018, **20**, 15030–15036.

108 W. Zhai, C. Tian, K. Yuan, C. Ge, S. Zhao, H. Yu, Y. Li, W. Chen and G. Ran, *Appl. Phys. Lett.*, 2019, **114**, 131107.

109 Y. Liang, Q. Shang, Q. Wei, L. Zhao, Z. Liu, J. Shi, Y. Zhong, J. Chen, Y. Gao, M. Li, X. Liu, G. Xing and Q. Zhang, *Adv. Mater.*, 2019, **31**, 1903030.

110 K. S. Nalwa, J. A. Carr, R. C. Mahadevapuram, H. K. Kodali, S. Bose, Y. Q. Chen, J. W. Petrich, B. Ganapathysubramanian and S. Chaudhary, *Energy Environ. Sci.*, 2012, **5**, 7042–7049.

111 H. S. Kim, S. K. Kim, B. J. Kim, K. S. Shin, M. K. Gupta, H. S. Jung, S. W. Kim and N. G. Park, *J. Phys. Chem. Lett.*, 2015, **6**, 1729–1735.

112 P. Wang, J. Zhao, L. Wei, Q. Zhu, S. Xie, J. Liu, X. Meng and J. Li, *Nanoscale*, 2017, **9**, 3806–3817.

113 L. You, F. Zheng, L. Fang, Y. Zhou, L. Z. Tan, Z. Zhang, G. Ma, D. Schmidt, A. Rusydi, L. Wang, L. Chang, A. M. Rappe and J. Wang, *Sci. Adv.*, 2018, **4**, eaat3438.

114 L. Qiao, W. H. Fang and R. Long, *J. Phys. Chem. Lett.*, 2019, **10**, 7237–7244.

115 C. C. Zhang, Z. K. Wang, S. Yuan, R. Wang, M. Li, M. F. Jimoh, L. S. Liao and Y. Yang, *Adv. Mater.*, 2019, **31**, 1902222.

116 T. Kumari, S. Jung, Y. Cho, H.-P. Kim, J. W. Lee, J. Oh, J. Lee, S. M. Lee, M. Jeong, J. M. Baik, W. Jo and C. Yang, *Nano Energy*, 2020, **68**, 104327.

This journal is © The Royal Society of Chemistry 2022

J. Mater. Chem. A, 2022, **10**, 19169–19183 | **19183**